ORIGINAL ARTICLE

Boualem Khouider · Andrew J. Majda

A non-oscillatory balanced scheme for an idealized tropical climate model

Part I: Algorithm and validation

Abstract We propose a non-oscillatory balanced numerical scheme for a simplified tropical climate model with a crude vertical resolution, reduced to the barotropic and the first baroclinic modes. The two modes exchange energy through highly nonlinear interaction terms. We consider a periodic channel domain, oriented zonally and centered around the equator and adopt a fractional stepping–splitting strategy, for the governing system of equations, dividing it into three natural pieces which independently preserve energy. We obtain a scheme which preserves geostrophic steady states with minimal ad hoc dissipation by using state of the art numerical methods for each piece: The f-wave algorithm for conservation laws with varying flux functions and source terms of Bale et al. (2002) for the advected baroclinic waves and the Riemann solver-free non-oscillatory central scheme of Levy and Tadmor (1997) for the barotropic-dispersive waves. Unlike the traditional use of a time splitting procedure for conservation laws with source terms (here, the Coriolis forces), the class of balanced schemes to which the f-wave algorithm belongs are able to preserve exactly, to the machine precision, hydrostatic (geostrophic) numerical-steady states. The interaction terms are gathered into a single second order accurate predictor-corrector scheme to minimize energy leakage. Validation tests utilizing known exact solutions consisting of baroclinic Kelvin, Yanai, and equatorial Rossby waves and barotropic Rossby wave packets are given.

Keywords Non-oscillatory balanced schemes · Barotropic-baroclinic nonlinear interactions · Precipitation fronts · Large scale equatorial waves

PACS 02.70.Bf; 02.30.Jr; 92.60.Bh; 92.60.Dj; 92.60.Jq

1 Introduction

There is an increasingly large interest among the atmospheric sciences community regarding the interactions between waves in the tropics and midlatitudes [1–9] as well as the effect of tropical waves on deep convection. In addition to addressing the issues of global pattern teleconnections between the equatorial region and the rest of the globe, the study of lateral energy exchange between the tropics and midlatitudes is also important for understanding the influence of the midlatitudes on tropical wave dynamics and their interaction with organized deep convective superclusters and many other tropical phenomena such as monsoons, the Madden-Julian oscillation, and EL Nino. Since a significant portion of the energy in the atmosphere is carried by the

B. Khouider (✉)
Mathematics and Statistics, University of Victoria, PO BOX 3045 STN CSC, Victoria, B.C., V8W 3P4, Canada
E-mail: khouider@math.uvic.ca

A. J. Majda
Department of Mathematics and Center for Atmosphere/Ocean Sciences, Courant Institute, New York University, 251 Mercer Street, New York, NY 10012, USA

barotropic mode which has an important projection on the midlatitudes, it is meaningful to address this issue through simplified models involving the interactions between the barotropic flow and the baroclinic-equatorial waves.

The studies of Webster [3–5], Kasahara and Silva Dias [6], Hoskins and Jin [7], etc. revealed the importance of both a horizontal and a vertical shear for the generation of a midlatitude response from a localized tropical heating source. Majda and Biello [1] have recently derived a simplified model for the nonlinear interactions between the equatorially trapped and the midlatitude Rossby waves by using a simple Galerkin projection of the beta-plane primitive equations onto the barotropic and the first vertical baroclinic modes. Through idealized examples, they showed how a barotropic Rossby wave packet can transfer its energy through a westerly wind burst into equatorially trapped Rossby waves in the presence of a baroclinic shear and vis versa. Furthermore, theoretical efforts in understanding convectively coupled tropical waves have focused on models with a crude vertical resolution involving a dominant baroclinic heating mode coupled to convection [10–15]. Such intermediate models are important as simplified models for several weeks to seasonal predictions as well as climate studies [16, 17]. They also provide a simplified analytical context to study various strategies for parametrizing convection [14, 18].

Perhaps, the most interesting phenomena in the tropics resides in the remarkable behavior of the equatorially trapped baroclinic waves [19, 20] which involve a mixture of dispersive and non-dispersive effects as well as their interaction with the barotropic Rossby wave packets in the presence of a vertical shear, as mentioned above. Also the wave propagation affects a great deal the large scale patterns of moisture, see, for example, the work of Wheeler and Kiladis in [21] and subsequent papers. Since the equatorial waves involve balanced as well as unbalanced dynamics, there is a large interest in developing simplified models which are capable of capturing the appropriate balanced dynamics and wave interaction across scales. Simplified balanced models used in the literature range from the family of Weak Temperature Gradient (WTG) models used by Sobel et al. [22] to the systematic multiscale models of Majda and Klein [23]. Especially, the more recent study by Frierson et al. [24] of the large scale precipitation fronts, using convective parametrization-like relaxation schemes, and their interactions with the equatorially trapped waves propagating in the heterogeneous moist/dry medium, inducing wave reflection and deflection at the front interfaces is more than fascinating.

The goal of this paper is to design a non-oscillatory[1] balanced numerical model for such intermediate climate models. We aim to build up a scheme which is very accurate on the scales of interest with a minimum ad hoc dissipation masking the interaction mechanisms and which is, at the same time, capable to capture (numerical) geostrophic steady states to machine precision. We use state of the art numerical methods in an appropriate combination to discretize different terms of the nonlinear barotropic-baroclinic model, derived by Majda and Biello [1] – following the strategy of Neelin and Zeng [17], in a periodic zonal channel centered at the equator, to which we apply a fractional stepping – operator splitting strategy.

The design of the numerical model and validation tests using known exact solutions, in the context of tropical dynamics is presented. The remaining parts of the paper are organized as follows. In Sect. 2, we discuss the simplified model as derived in [1] by Galerkin projecting the nonlinear beta-plane primitive equations onto the barotropic and the first baroclinic modes. The interacting systems are then augmented by and coupled to a vertically averaged moisture equation. We then show an energy conservation principle for the dry system, which is exploited in Sect. 3, to formulate our basic discretization strategy, consisting of fractional stepping, for the system of governing equations, dividing it into three major pieces which conserve their own energies: A linear system for the advected equatorial-baroclinic waves, an incompressible system for the dispersive barotropic Rossby waves, and the third part gathers the interaction terms into a single system. This is then followed by a short discussion of the discretization of the interaction system coupling the barotropic and baroclinic subsystems, which constitute the hard core of the code.

The discretization of the advected baroclinic waves is discussed and validated in Sect. 4. We use the well-balanced f-wave algorithm of Bale et al. [25], which is especially designed for conservation laws with varying flux functions and source terms. Particular care is taken for the boundary conditions at the channel walls to minimize both the wave reflection and the leakage of energy at the wall boundaries. Well balanced schemes are commonly used in the compressible flows community for the accurate resolution of conservation laws with source terms near steady states. More on well-balanced schemes can be found in [25–28], and references therein. The f-wave method is chosen here for both its pedagogical and implementation simplicity,

---

[1] The adjective non-oscillatory is intended to describe the ability of the numerical scheme to resolve shocks and steep gradients instead of perhaps, the more adequate 'high-resolution' term which is used in the compressible fluids community. The latter is avoided here because it could lead to confusion with other meanings such as 'fine-grid' as it is used in the atmospheric modeling community.

its robustness, and its ability of handling spatially dependent flux-functions. In Sect. 5 we carefully adapt the non-oscillatory central scheme of Levy and Tadmor [29], developed for the incompressible Euler equations, to discretize the barotropic system with dispersive waves. This is followed by validation tests using Rossby wave packets where some issues, associated with the special case of the channel geometry, such as the conditions at the wall boundaries are addressed.

A concluding discussion is given in Sect. 6 while some technical details of the wave propagation method of R. LeVeque are given in the Appendix at the end.

2 The simplified climate model

2.1 The barotropic-first baroclinic model with moisture

We consider the primitive equations on a beta-plane with rigid lid boundary conditions.

$$
\begin{align*}
\text{(A)} \quad & \frac{D\mathbf{V}_H}{Dt} + \beta y \mathbf{V}_H^{\perp} = -\nabla_H P + \mathcal{S}_{\mathbf{v}} \\
\text{(B)} \quad & \mathrm{div}_H \mathbf{V}_H + W_z = 0 \\
\text{(C)} \quad & \frac{D\Theta}{Dt} + \frac{N^2\theta_0}{g}W = \mathcal{S}_\Theta \\
\text{(D)} \quad & \frac{\partial P}{\partial z} = g\frac{\Theta}{\theta_0} \\
\text{(E)} \quad & W|_{z=0,H_T} = 0.
\end{align*}
\tag{2.1}
$$

Here $\mathbf{V}_H = (U, V)$ is the horizontal velocity, W is the vertical velocity, P is the pressure, and Θ is the potential temperature. Capital letters are used in order to distinguish the total quantities represented in the primitive equations in (2.1) from their Galerkin projection components which are introduced below. Notice that in (2.1), according to the Boussinesq approximation, the density is assumed constant, and the equations are normalized accordingly, except for the buoyancy acceleration in (D) where, in addition, the hydrostatic balance and the ideal gas law are used. Here $N = 0.01$ s^{-1} is the Brunt-Vaisala buoyancy frequency, $g = 9.8$ m s^{-2} is the gravitational acceleration, and $\theta_0 = 300$ K is a reference (constant background) potential temperature. $\beta = 2.2804 \times 10^{-11}$ s^{-1}m^{-1} is the gradient of the Coriolis force at the equator. Also

$$
\frac{D}{Dt} \equiv \frac{\partial}{\partial t} + U\frac{\partial}{\partial x} + V\frac{\partial}{\partial y} + W\frac{\partial}{\partial z}
$$

is the material derivative while div_H, ∇_H are the horizontal divergence and horizontal gradient, respectively. $\mathbf{V}_H^{\perp} = (-V, U)$ and $\mathcal{S}_{\mathbf{v}}$, $\mathcal{S}_\theta$ represent sources and sinks of momentum and heat, respectively, e.g., Rayleigh friction and convective heating and/or radiative cooling. Typically, the detailed moist dynamics are obtained by coupling the equations in (2.1) to the bulk cloud microphysics equations by invoking the budget equations of the moisture variables such as cloud water, water vapor, and rain (see for eg. [24] for details). Here, for simplicity, we skip this and present below rather directly the equation for the vertically averaged total water content, q, coupled to the barotropic-first baroclinic equations, which are presented next. The barotropic-first baroclinic equations were derived by Majda and Biello [1] by a simple vertical Galerkin projection of the nonlinear primitive equations in (2.1) onto the barotropic and the first baroclinic modes [20] following the strategy of Neelin and Zeng [17]. Now we summarize briefly the Galerkin derivation of Majda and Biello for the sake of completeness. The barotropic mode is obtained by a simple vertical averaging over the tropospheric height, $H_T \approx 16$ km, of the equations in (2.1) while the projection onto the first baroclinic mode is achieved by taking the functional inner product,

$$
\langle f, g \rangle = \frac{1}{H_T}\int_0^{H_T} f(z)g(z)\,\mathrm{d}z,
$$

with $g = \cos(\frac{z\pi}{H_T})$ for the case of the horizontal velocity, $\mathbf{V}_H$, and the pressure, P, and $g = \sin(\frac{z\pi}{H_T})$ for the potential temperature, Θ, and the vertical velocity, W, i.e, the following crude vertical approximation is made

[1, 15, 20], etc.

$$\begin{pmatrix} \mathbf{V}_H \\ P \end{pmatrix}(x, y, z, t) \approx \begin{pmatrix} \overline{\mathbf{v}} \\ \overline{p} \end{pmatrix}(x, y, t) + \begin{pmatrix} \mathbf{v} \\ p \end{pmatrix}(x, y, t) \cos\left(\frac{\pi z}{H_T}\right)$$

$$\begin{pmatrix} W \\ \Theta \end{pmatrix}(x, y, z, t) \approx \begin{pmatrix} w \\ \theta \end{pmatrix}(x, y, t) \sin\left(\frac{\pi z}{H_T}\right). \tag{2.2}$$

Notice that because of the rigid-lid condition in (2.1) (E) and the hydrostatic balance in (2.1) (D), the barotropic components of both the vertical velocity and the potential temperature vanish. The hydrostatic equation links the baroclinic components of the pressure and the potential temperature,

$$p = -\frac{g H_T \theta}{\pi \theta_0},$$

while the vertical velocity is recovered through the continuity equation,

$$w = -\frac{H_T}{\pi} \mathrm{div} \mathbf{v}.$$

The various dynamical variables, $\overline{\mathbf{v}}, \overline{p}, \mathbf{v}, \theta$, are converted to non-dimensional quantities by using the following reference scales, relevant to the tropical wave dynamics [15, 19, 20, etc]: the gravity wave speed $c = N H_T/\pi \approx 50$ m/s is used as the velocity scale, the equatorial Rossby deformation radius $L = (c\beta^{-1})^{1/2} \approx 1500$ km as the length scale, $T = L/c \approx 8$ hours as the time scale, and $\bar{\alpha} = \frac{H_T N^2 \theta_0}{\pi g} \approx 15$ K is our temperature scale. Therefore, the barotropic-baroclinic nonlinear interacting system resulting from the Galerkin projection strategy above, in nondimensional units, simplifies to [1]

$$\frac{\partial \overline{\mathbf{v}}}{\partial t} + \overline{\mathbf{v}} \cdot \nabla \overline{\mathbf{v}} + y\overline{\mathbf{v}}^\perp + \nabla \overline{p} = -\frac{1}{2}\left(\mathbf{v} \cdot \nabla \mathbf{v} + \mathbf{v} \mathrm{div} \mathbf{v}\right)$$

$$= -\frac{1}{2}\mathrm{div}\left(\mathbf{v} \otimes \mathbf{v}\right)$$

$$\mathrm{div}\overline{\mathbf{v}} = 0 \tag{2.3}$$

and

$$\frac{\partial \mathbf{v}}{\partial t} + \overline{\mathbf{v}} \cdot \nabla \mathbf{v} - \nabla \theta + y\mathbf{v}^\perp = -\mathbf{v} \cdot \nabla \overline{\mathbf{v}}$$

$$\frac{\partial \theta}{\partial t} + \overline{\mathbf{v}} \cdot \nabla \theta - \mathrm{div} \mathbf{v} = \mathcal{S}(x, y, t) \tag{2.4}$$

The momentum friction/forcing terms are ignored for simplicity and $\mathcal{S}(x, y, t)$ denotes the projection of $\mathcal{S}_\Theta$ in (2.1) onto the first heating mode.

In order to get a closure for the source term, $\mathcal{S}(x, y, t)$, in (2.4), we introduce next the equation governing the vertically integrated moisture content, q, with a prescribed background moisture gradient.

$$\frac{\partial q}{\partial t} + \overline{\mathbf{v}} \cdot \nabla q + \tilde{Q} \mathrm{div} \mathbf{v} = -\mathcal{P} + E \tag{2.5}$$

where $\mathcal{P}$ is the precipitation rate, E is the surface evaporative flux, and

$$\tilde{Q} = \bar{Q} L_c \frac{2H_T}{\pi^2}, \tag{2.6}$$

where $L_c \approx 188$ is a dimension-less rescaling constant involving the latent heat of vaporization which permits one to convert moisture quantities into temperature units and $\bar{Q}$ is the actual background moisture gradient, imposed over a *moisture scale height* which is taking here to be equal to the total tropospheric height, H_T. For a detailed discussion on (2.5), we refer the interested reader to [24]. A rigorous derivation involving an arbitrary *moisture scale height* will be published elsewhere by the authors.

The system formed by (2.3), (2.4) is coupled to the equation in (2.5) through the source term $\mathcal{S}$ and the precipitation rate, $\mathcal{P}$, which are parametrized together as functions of both the potential temperature and the moisture content variables θ and q. Typically, we write

$$\mathcal{S} = \mathcal{C} - Q_R \tag{2.7}$$

where $\mathcal{C}$ is the convective heating which is proportional to the precipitation rate $\mathcal{P}$ and Q_R is a Newtonian cooling term. In the remaining of this paper, we drop the moisture equation and with it the convective forcing terms and concentrate ourselves on the design of a non-oscillatory balanced numerical scheme for the dry system formed by (2.3) and (2.4). We shall return to the moisture equation and to the convective-like forced system in Part II of this series of papers.

2.2 Conservation of total energy for the dry system in a channel

As already stated in [1], here we show that under the no-flow boundary conditions at the channel walls, the coupled system in (2.3), (2.4) conserves energy in the absence of 'external' forcing. We consider the dry system formed by (2.3), (2.4) with $\mathcal{S} \equiv 0$ in a zonally oriented periodic channel. The north-south walls are located at a distance $Y = 5000$ km away from the equator and the zonal period is equal to the perimeter of the earth at the equator, i.e, $X = 40\,000$ km. We assume a no-flow boundary condition at the channel walls for both the barotropic and the baroclinic flows, to contain the fluid inside the channel.

$$\overline{\mathbf{v}}(x, \pm Y, t) = 0, \ \mathbf{v}(x, \pm Y, t) = 0. \tag{2.8}$$

Let

$$\mathcal{E}_C(t) = \frac{1}{4} \int_{-Y}^{Y} \int_0^X |\mathbf{v}|^2 + \theta^2 \, \mathrm{d}x \mathrm{d}y \tag{2.9}$$

be the total (kinetic + potential) energy associated with the baroclinic flow and

$$\mathcal{E}_T(t) \equiv \frac{1}{2} \int_{-Y}^{Y} \int_0^X |\overline{\mathbf{v}}|^2 \, \mathrm{d}x \mathrm{d}y \tag{2.10}$$

be the kinetic energy associated with the barotropic flow. Note that the peculiar factor of 1/4 in the total energy in (2.9) arises from the fact that the vertical projection in (2.2) omits a $\sqrt{2}$ factor and therefore is not a unit eigenvector decomposition. Then, under the boundary conditions in (2.8), as pointed out in [1], the total (dry) energy defined by

$$\mathcal{E}_d(t) \equiv \mathcal{E}_C(t) + \mathcal{E}_T(t) \tag{2.11}$$

is conserved. In fact, we have

$$\frac{d}{dt} \mathcal{E}_C(t) = -\frac{1}{2} \int_0^X \int_{-Y}^Y \mathbf{v} \otimes \mathbf{v} \cdot \nabla \overline{\mathbf{v}} \, \mathrm{d}x \mathrm{d}y.$$

and

$$\frac{d}{dt} \mathcal{E}_T(t) = -\frac{1}{2} \int_0^X \int_{-Y}^Y \overline{\mathbf{v}} \cdot \mathrm{div} \, (\mathbf{v} \otimes \mathbf{v}) \, \mathrm{d}x \mathrm{d}y.$$

Which leads to

$$\frac{d}{dt} \mathcal{E}_d(t) = -\frac{1}{2} \int_0^X \int_{-Y}^Y \mathrm{div} \, [(\mathbf{v} \otimes \mathbf{v}) \overline{\mathbf{v}}] \, dx dy = 0 \text{ by (2.8)}.$$

Notice that if the interaction terms on the right hand-sides of (2.3) and (2.4) are zero, then the first two time derivatives above vanish, i.e., both the baroclinic and the barotropic systems in (2.3) and (2.4), respectively, conserve their own energy when their mutual interaction is ignored. Therefore, the energy of interaction is also conserved. This is what is actually exploited below to design a non-oscillatory balanced scheme with a minimum ad hoc dissipation.

3 The basic discretization strategy

3.1 Time splitting algorithm in continuous form

Now we take advantage of the way the coupled system in (2.3) and (2.4) conserves the different forms of energy, as discussed above, to design a time splitting (fractional step) algorithm where the baroclinic-barotropic interaction system is broken into three pieces which individually conserve energy. The resulting subsystems are then discretized and coded into three different routines, which are called separately in the code. The resulting systems are given next, in continuous form. They consist of

– a linear conservation system for the advected baroclinic waves

$$\frac{\partial \mathbf{v}}{\partial t} + \text{div} \, (\overline{\mathbf{v}} \otimes \mathbf{v}) - \nabla \theta + y\mathbf{v}^\perp = 0$$
$$\frac{\partial \theta}{\partial t} + \nabla \cdot (\overline{\mathbf{v}}\theta) - \text{div}\mathbf{v} = 0, \tag{3.1}$$

– a nonlinear incompressible system for the barotropic waves

$$\frac{\partial \overline{\mathbf{v}}}{\partial t} + \overline{\mathbf{v}} \cdot \nabla \overline{\mathbf{v}} + y\overline{\mathbf{v}}^\perp = -\nabla \overline{p}$$
$$\nabla \cdot \overline{\mathbf{v}} = 0, \tag{3.2}$$

– and a third system gathering the coupled nonlinear interaction terms into a single coupled system. The latter is given below in terms of the potential vorticity.

3.2 Remarks on the partial discretizations and on the numerical boundary conditions

Notice that because the barotropic-advecting flow is incompressible, the system in (3.1) is alternatively written in conservative form. This is also exploited below for the barotropic piece in (3.2). The discrete system resulting from (3.1) is closed with the aide of the periodic boundary conditions in x and homogeneous Dirichlet boundary conditions at $y = \pm Y$ which are compatible with the no-flow condition in (2.8) as well as non-reflecting and extrapolation with the exact solution, for validation purposes, as described below in Sect. 4.

In order to conserve geostrophy (numerically), for the barotropic system in (3.2), we pass to the potential vorticity-stream function formulation. We introduce the potential vorticity

$$\overline{\xi} = \overline{v}_x - \overline{u}_y + y$$

and the stream function

$$\overline{u} = -\overline{\psi}_y; \ \overline{v} = \overline{\psi}_x.$$

The system in (3.2) leads to

$$\frac{\partial \overline{\xi}}{\partial t} + \overline{u}\frac{\partial \overline{\xi}}{\partial x} + \overline{v}\frac{\partial \overline{\xi}}{\partial y} = 0$$
$$\Delta \overline{\psi} = \overline{\xi} - y \tag{3.3}$$
$$\overline{u} = -\overline{\psi}_y; \ \overline{v} = \overline{\psi}_x.$$

Since, according to the first equation in (3.3) and the divergence constraint, the potential vorticity, $\overline{\xi}$, is conserved, numerical geostrophic balance for the barotropic flow is automatically guaranteed provided we use a conservative scheme to discretize the conservation law.

The continuous system in (3.3) is seemingly closed by the periodic boundary conditions in x and the no-flow ($\overline{v} = 0$) condition at the channel walls. However, for the discrete version, some numerical values are needed at the ghost cells outside the walls, for the potential vorticity, $\overline{\xi}$, and they have to be 'chosen' carefully. Particularly, we demonstrate in Sect. 5, below, that homogeneous Dirichlet boundary conditions do a better job than the popular polynomial extrapolation ones which tend to create a numerical boundary layer near the walls where vorticity is generated and is amplified in time.

In terms of the vorticity-stream function formulation, we have for the interaction system

$$\frac{\partial \overline{\xi}}{\partial t} = -\frac{1}{2} \left(\left(\frac{\partial^2}{\partial x^2} - \frac{\partial^2}{\partial y^2} \right)(uv) + \frac{\partial^2}{\partial x \partial y} \left(v^2 - u^2 \right) \right)$$

$$\frac{\partial \mathbf{v}}{\partial t} = -\mathbf{v} \cdot \nabla \overline{\mathbf{v}}$$

$$\Delta \overline{\psi} = \overline{\xi} - y \tag{3.4}$$

$$\overline{u} = -\overline{\psi}_y; \ \overline{v} = \overline{\psi}_x, \quad \mathbf{v} = (u, v), \quad \overline{\mathbf{v}} = (\overline{u}, \overline{v})$$

For consistency, when discretized, the system in (3.4) is closed by the same boundary conditions as inherited from (3.1) and (3.3).

Recall that at each fractional step, only one among the three sub-systems in (3.1), (3.3), and (3.4) is integrated independently while the others are frozen. Especially, the integration of the system in (3.1), from time t to time $t + \Delta t$, assumes that the advecting-barotropic flow $(\overline{u}, \overline{v})$ is constant on the interval $[t, t + \Delta t]$. Here $\Delta t > 0$ is the time step, common to the three systems, based on a CFL condition accounting for both the advective-barotropic flow as well as for the dry gravity wave speed of 50 m/s. This splitting strategy is consistent, by many means, with the use of the f-wave method for conservation laws with space dependent flux functions but autonomous in time, in Sect. 4, for the baroclinic system. This method is introduced by LeVeque and his collaborators [25] to handle flux-varying conservation laws with source terms. It leads to a non-oscillatory geostrophically balanced second order numerical scheme for the advected-baroclinic waves system in (3.1). For the potential vorticity-stream function system in (3.3) we use the non-oscillatory central scheme, introduced by Levy and Tadmor in [29] for the 2d incompressible Euler equations (see [30] for a variant of the method which deals directly with the momentum formulation).

Before moving forward to discussing the details of the numerical schemes used for solving the subsystems in (3.1) and (3.3), which constitute the hard-core of the present code, we will first design a second order scheme for solving the energy conserving interaction system in (3.4). For the latter, we use central finite differences in space coupled with a predictor corrector method in time.

3.3 A second order discretization for the interaction system

The spatial derivatives on the right-hand side of the evolution equations in (3.4) are discretized by centered differences, using a five point stencil so that

$$\frac{\partial^2 f}{\partial x^2} \approx \frac{f_{i+1,j} - 2f_{i,j} + f_{i-1,j}}{\Delta x^2}, \ \frac{\partial^2 f}{\partial y^2} \approx \frac{f_{i,j+1} - 2f_{i,j} + f_{i,j-1}}{\Delta y^2},$$

and $\quad \dfrac{\partial^2 f}{\partial x \partial y} \approx \dfrac{f_{i+1,j+1} - f_{i-1,j+1} - f_{i+1,j-1} + f_{i-1,j-1}}{4 \Delta x \Delta y}. \tag{3.5}$

The discrete incompressible barotropic flow is tied to the evolving potential vorticity, $\overline{\xi}_{i,j}$, through the discrete stream function, $\overline{\psi}_{i,j}$, by a five-point Poisson solver. The discrete barotropic velocity field is obtained by 2nd order centered differences so that it remains incompressible as in Sect. 5 below. The time integration is performed via a 2nd order Runge-Kutta type predictor-corrector method, applied to the semi-discrete version of (3.4), obtained by substituting the finite differences in (3.5) into the spatial derivatives.

3.4 Alternate discretization

Before we end this section, it is worthwhile mentioning that other-alternate splitting strategies are possible. A somewhat natural splitting strategy, which will also yield energy conserving subsystems, would be obtained by moving the advection terms in (3.1) into the system in (3.3) so that the new system, which is accordingly augmented with the advection equations for $\mathbf{v}$ and θ, would be solved as a whole by the central scheme of Levy and Tadmor (in Sect. 5); leaving a simple linear shallow water system in (3.1) which can be solved by any well balanced solver, eg. [26–28]. Nevertheless, the splitting strategy keeping the advection terms in (3.1) is justified in part by: 1) the f-wave algorithm in [25] is originally designed to handle conservation laws with varying fluxes, 2) the flows of interest are 'subsonic' (the velocity maximum is below the gravity wave speed); therefore, the system in (3.1) remains strictly hyperbolic, and more importantly 3) we want to capture the geostrophic balance with respect to a background advecting barotropic flow as well.

4 A balanced non-oscillatory method for equatorial baroclinic waves

As mentioned above we now use the f-wave algorithm of Bale et al. [25] to descritize the advected shallow water system in (3.1). This results in a robust non-oscillatory 2nd order scheme with the property that initial geostrophic steady states will remain so during the discrete integration; even in the presence of a barotropic wind.

The f-wave algorithm came as a generalization and an improvement, for conservation laws with varying flux functions, of the quasi-steady wave-propagation method proposed by LeVeque in [26] to compute (non-linear) shallow water flows which are near hydrostatic balance with respect to topographic source terms. A more sophisticated approach, which also conserves dry beds, is introduced and used in [27, 28]. This method makes the systematic use of left and right states to solve the Riemann problem directly while LeVeque's wave propagation method is based on the flux differences, i.e., it assumes a Roe-like numerical scheme. Furthermore, the non-oscillatory version of LeVeque's scheme is obtained through the flux-limiting strategy while the former uses the slope-limiting technique. Nevertheless, because the f-wave algorithm is originally designed and easily implemented for one-space-dimension systems, (3.1) is further split onto two unidimensional systems for each direction x and y, respectively.

4.1 Dimensional operator splitting

It is common to use the dimensional operator splitting strategy for the multi-dimensional shallow water equations such as (3.1) [26, 28, etc.], permitting the advance in time of each direction separately. This is done in such a fashion that the Coriolis terms are distributed onto the resulting 1d systems so that both the meridional and zonal velocities, v, u, are decoupled from the x- and y-systems into two simple linear-advection equations in the x- and y-directions, respectively. Namely, (3.1) is decomposed onto the following two 1d systems:

$$\frac{\partial u}{\partial t} + \frac{\partial (\overline{u}u)}{\partial x} - \frac{\partial \theta}{\partial x} - yv = 0$$
$$\frac{\partial \theta}{\partial t} + \frac{\partial (\overline{u}\theta)}{\partial x} - \frac{\partial u}{\partial x} = 0 \qquad (4.1)$$
$$\frac{\partial v}{\partial t} + \frac{\partial (\overline{u}v)}{\partial x} = 0$$

and

$$\frac{\partial v}{\partial t} + \frac{\partial (\overline{v}v)}{\partial y} - \frac{\partial \theta}{\partial y} + yu = 0$$
$$\frac{\partial \theta}{\partial t} + \frac{\partial (\overline{v}\theta)}{\partial y} - \frac{\partial v}{\partial y} = 0 \qquad (4.2)$$
$$\frac{\partial u}{\partial t} + \frac{\partial (\overline{v}u)}{\partial y} = 0.$$

Notice that in order to guarantee second order accuracy a Strang-splitting procedure is needed when the routines for solving (4.1) and (4.2) are individually called in the code. Furthermore, it is demonstrated, for the case of the equatorial waves here (results not shown), that the Strang-splitting procedure, as opposed to the classical fractional step method which is only first order is required even for the directional splitting in (4.1) and (4.2), in order to recover the second order accuracy. Particularly, the L1 error is improved by one order of magnitude on the coarse mesh of 128×75 grid points. This finding is in itself interesting because it is often argued in the literature that the Strang's strategy is not necessary for the dimensional splitting on the grounds that this latter induces only small errors which are negligible compared to the errors induced by the partial discretizations of the mono-directional systems.

4.2 The f-wave algorithm with source term

The f-wave algorithm is introduced in [25] as an improvement and a generalization of the wave propagation algorithm in [26] to handle conservation laws with spatially varying flux functions and source terms (balance

laws). The f-wave algorithm as opposed to the original wave propagation algorithm decomposes the flux increments, $F(U_{i+1}) - F(U_i)$, directly into simple waves instead of passing by the decomposition of the increments, $U_{i+1} - U_i$, as the original algorithm does. Because it is actually the flux increments and not the wave increments which are needed and which are used within the code to update the state variables. The new algorithm avoids the unnecessary calculations permitting the passing from the individual waves to an approximation of the flux differences which makes the new method more robust and more efficient. Nevertheless, it has the same implementation pattern as the original wave propagation algorithm including its second order extension. Perhaps the most important advantage of the f-wave algorithm resides in its ability to handle balanced laws near steady states with high accuracy. It suffices to incorporate the source terms into the flux increment before the wave decomposition is performed. Therefore, it is only the deviation of the (computed) solution from steady state which is decomposed into waves so that steady states are automatically preserved since, in this case, the strength of the waves resulting from a (numerically) balanced state would be zero. The reader is referred to [25, 26] and references therein. Nevertheless, we give next a brief summary for the sake of completeness.

To illustrate, we consider the following generic conservation law system with source term (balance law).

$$\frac{\partial U}{\partial t} + \frac{\partial F(x, U)}{\partial x} + B(U) = 0. \tag{4.3}$$

Here $F(x, U)$ is a vector valued spatially varying flux function pointing toward the conservative part of either one of the systems in (4.1) and (4.2) while the term $B(U)$ points toward the Coriolis force terms $-yv$ and yu, respectively.

4.3 F-wave algorithm for conservation laws

As pointed out above the f-wave algorithm of Bale et al. [25] comes as a generalization and improvement of the f-wave algorithm of R. LeVeque [26]; therefore, we believe that, for pedagogical reasons, it is important to give a short summary of the wave-propagation method first. However, in order to streamline this article, the short summary is in Appendix A. The non-expert is encouraged to read that appendix before continuing with the rest of this section. For the generic conservation law

$$U_t + F(U) = 0,$$

the f-wave algorithm of Bale et al. [25] proceeds in the same manner as in the wave-propagation algorithm [26] of decomposing into individual waves the left and right going fluxes at the cell edges $i + 1/2$. The main and somewhat the only technical difference between the two schemes resides in the fact that the new algorithm uses instead a decomposition of the flux increments directly. Namely, we let

$$F(U_{i+1}) - F(U_i) = \sum_{p=1}^{M} \beta_p R_p = \sum_{p=1}^{M} \mathcal{Z}_{i+1/2}^p$$

where R_p's are the eigenvalues of the approximate Jacobian matrix at the cell edges $i + 1/2$. Nevertheless, the new algorithm yields a conservative scheme even if the associated Roe scheme is not conservative, and it is especially designed to perform on conservation laws with varying flux functions, as it is the case for the advected baroclinic systems in (4.1) and (4.2). More importantly, for the case of balanced laws, the f-wave algorithm yields easily a balanced scheme by directly incorporating the source term into the flux differences at the cell interfaces, before the wave decomposition is performed, as summarized below.

To some extent, the f-wave algorithm can be viewed as an new way of rewriting the original wave propagation algorithm. This is true at least for the linear case for which we have

$$F(U_i) - F(U_{i-1}) = \sum_{p=1}^{M} \mathcal{Z}_{i-1/2}^p = \sum_{p=1}^{M} \alpha_p \lambda_{i-1/2}^p R_{i-1/2}^p = \sum_{p=1}^{M} \lambda_{i-1/2}^p \mathcal{W}_{i-1/2}^p$$

$$\text{with } \alpha_p = \begin{cases} \frac{\beta_p}{\lambda^p}, & \lambda^p \neq 0 \\ 0, & \lambda^p = 0 \end{cases} \quad p = 1, 2, \cdots M$$

and $\lambda_{i-1/2}^p$'s are the eigenvalues of the approximate Jacobian matrix and $\mathcal{W}_{i-1/2}^p$ are the individual or simple waves computed through the Riemann invariants at the interfaces $i - 1/2$. Therefore its implementation follows directly from the wave propagation algorithm and particularly the second order flux corrections are given by

$$\tilde{F}_{i-1/2} = \frac{1}{2} \sum_{p=1}^{M} \left(1 - \frac{\Delta t}{\Delta x} |\lambda_{i-1/2}^p| \right) \text{sign}(\lambda_{i-1/2}^p) Z_{i-1/2}^p.$$

4.4 F-wave algorithm for balance laws

In the presence of source terms like in (4.3), the f-wave algorithm leads easily to a balanced scheme where numerical steady states are captured and preserved exactly to the machine precision. The source term is first distributed onto delta functions defined on the cell edges so that it is rather the flux difference plus the source term, as a whole, which is decomposed onto waves

$$F(U_{i+1}) - F(U_i) + \Delta x B(U_{i+1/2}) = \sum_{p=1}^{M} \mathcal{Z}_{i+1/2}^p$$

where $B(U_{i+1/2})$ is some adequate approximation of $B(U)$ at the cell edges $i + 1/2$ (e.g., $B(U_{i+1/2}) = (B(U_i) + B(U_{i+1}))/2$). In this fashion, a (discrete) steady state ($F(U_{i+1}) - F(U_i) + \Delta x B(U_{i+1/2}) = 0$) will result in a decomposition into waves with zero strengths.

In order to get a second order scheme for the balanced scheme, the following correction term needs to be added into the updating formula in (A4) [25]

$$\frac{(\Delta t)^2}{2\Delta x} \frac{\partial B(U_i)}{\partial U} \sum_{p=1}^{M} \frac{\mathcal{Z}_{i+1/2}^p + \mathcal{Z}_{i-1/2}^p}{2}.$$

4.5 Numerical boundary conditions at the walls

While the periodic boundary conditions for the x-direction system in (4.1) are easily implemented, the handling of the boundary conditions at the artificial walls during the implementation of the y-direction system in (4.2) is a serious numerical issue. Below we propose and, later on, compare three types of boundary conditions for (4.2).

The first type of boundary conditions we consider here is based on a wave-non-reflection principle which consists of not allowing outgoing waves to be reflected into the domain. This type of boundary conditions is particularly suitable when artificial walls are imposed within the body of the fluid to delimit the computational domain which is otherwise infinite. In order for a one way-wave equation to be well-posed, no boundary condition should be imposed on the artificial wall where the wave is going outward but a boundary condition is required at the wall where the information is inward [31]. It is this idea which is exploited and expanded to the shallow water equations by the aide of the Riemann invariants [31]. Since by (2.8) the barotropic meridional wind $\bar{v}$ is set to zero at the walls, (4.2) simplifies to

$$\frac{\partial v}{\partial t} - \frac{\partial \theta}{\partial y} + yu = 0$$
$$\frac{\partial \theta}{\partial t} - \frac{\partial v}{\partial y} = 0 \qquad\qquad (4.4)$$
$$\frac{\partial u}{\partial t} = 0.$$

at $y = \pm Y$. The last equation suggests that, except for variations due to the x-system in (4.1), u is constant in time at the channel walls. Hence any type of boundary conditions can be imposed on u when solving (4.2). Next we introduce the Riemann invariants for the system formed by v and θ,

$$r^+ = v - \theta; \quad r^- = v + \theta$$

which satisfy

$$\frac{\partial r^{\pm}}{\partial t} \pm \frac{\partial r^{\pm}}{\partial y} + yu = 0. \tag{4.5}$$

Given $r^{\pm}$ at time $t = 0$, the exact solutions for (4.5) at times $t > 0$ is given by [32]

$$r^{\pm}(y, t) = r^{\pm}(y \mp t, 0) - \int_0^t (y \mp (s - t))u(y \mp (s - t), s) \, ds;$$

If we use a zero order extrapolation for u to the ghost cells outside the walls, then from the exact formula for r^+ above we get, for example at the south wall, $y = -Y$,

$$r^+(y, t) = r^+(y - t, 0) - u(-Y) \int_0^t (y - (s - t)) \, ds = r^+(y - t, 0) - u(-Y)\left(yt + \frac{1}{2}t^2\right)$$

By imposing the radiation condition $r^+(., 0) \equiv 0$ outside the domain so that no energy is injected into the domain from outside, we get

$$r^+(y, t) = -u(-Y)(yt - t^2)$$

and since r^- is propagating southward, we make the zero order extrapolation $r^-(y, 0) \equiv r^-(-Y, 0)$, for $y < -Y$, which leads to

$$r^-(y, t) = r^-(-Y, 0) - u(-Y)(yt - \frac{1}{2}t^2).$$

By using similar arguments at the north wall, we get the following

> *BC#1: Non-reflecting boundary conditions*
> $u(y, t) = u(-Y, 0), \ r^+(y, t) = -y\Delta tu(-Y, 0),$
> and $r^-(y, t) = r^-(-Y, 0) - y\Delta tu(-Y, 0)$ if $y < -Y$
> $u(y, t) = u(Y, 0), \ r^+(y, t) = r^+(Y, 0) - y\Delta tu(Y, 0),$
> and $r^-(y, t) = -y\Delta tu(Y, 0)$ if $y > Y$ $\hfill(4.6)$

within the time step Δt where we dropped the terms involving the second powers of t.

The second type of boundary conditions we are interested in is the homogeneous (fixed) Dirichlet boundary conditions. This type of boundary conditions is motivated by the solid wall conditions imposed in (2.8) to ensure energy conservation for the channel geometry.

> *BC#2: Homogeneous Dirichlet BC for all the variables, u, θ, v:*
> $u(y) = 0, \ v(y) = 0, \theta(y) = 0, \ \ \text{if } y < -Y \text{ or } y > Y. \hfill(4.7)$

Finally, the third type of boundary condition of interest here is derived by fixing the values of u, θ, v to the exact analytical solution. This is of course impractical because we are not supposed to know the solution of the problem before hand, but it turns out to be very useful when it comes to making validation tests.

> *BC#3: Exact solution for validation*
> The numerical solution at the ghost cells outside the walls is fixed to its exact
> analytical value there, i.e., Dirichlet boundary condition using the exact solution.

4.6 Validation tests

Now we propose to validate the balanced algorithm proposed above for the linear beta-plane equatorial shallow equations by using the large scale equatorial waves, well known among the atmospheric science community [19, 20]. These are exact solutions for the baroclinic system in (3.1) in the absence of the barotropic advection ($\bar{\mathbf{v}} \equiv 0$). Especially, we demonstrate that the f-wave scheme is capable of capturing accurately the geostrophic balanced as well as the unbalanced waves. In particular, we consider the following large scale equatorial waves [19, 20]. The Kelvin wave,

$$u(x, y, t) = \cos\left(2\pi \frac{x-t}{X}\right) e^{-y^2/2}, \ v(x, y, t) = 0, \ \theta(x, y) = -u(x, y, t), \tag{4.8}$$

where X is the perimeter of the equator expressed in non-dimensional units, which is perfectly geostrophically balanced in the meridional direction since the meridional flow, v, is zero. The Yanai wave, which is given by

$$
\begin{aligned}
v(x, y, t) &= \cos(kx - \omega t)\exp(-y^2/2); \\
u(x, y, t) &= -\omega y \exp(-y^2/2)\sin(kx - \omega t); \\
\theta(x, y, t) &= -\frac{1}{\bar{\alpha}}u(x, y, t))
\end{aligned}
\tag{4.9}
$$

where $\omega = (\frac{2\pi}{X} + \sqrt{\frac{4\pi^2}{X^2} + 4})/2$ is the phase of the wave and $k = 2\pi/X$ is the wavenumber, has a strong cross equatorial flow thus it provides a (strongly) unbalanced test case. Finally, the anti-symmetric equatorial Rossby wave of index 2 (MI= 2),

$$
\begin{aligned}
v(x, y, t) &= (2y^2 - 1)e^{-y^2/2}\cos(kx - \omega t) \\
r^+(x, y, t) &= \frac{4y^3 - 6y}{k - \omega}e^{-y^2/2}\sin(kx - \omega t) \\
r^-(x, y, t) &= -\frac{4y}{k + \omega}e^{-y^2/2}\sin(kx - \omega t)
\end{aligned}
\tag{4.10}
$$

with ω is the smallest in magnitude root of the dispersion relation

$$\omega^2 - k^2 - \frac{k}{\omega} = 5$$

and $r^+ = u - \theta$, $r^- = u + \theta$ are the Riemann invariants introduced above; this last example is chosen because it constitutes a weakly balanced solution according to the long wave approximation theory [19, 20]. Furthermore, notice that the Kelvin wave is non-dispersive, while the Yanai and MI = 2 Rossby waves are dispersive and the Kelvin wave and Yanai wave, with regards to the meridional velocity v, are symmetric with respect to the equator while the MI = 2 Rossby wave is anti-symmetric. Thus, these three exact solutions form a set of tests which is representative of the equatorial baroclinic (linear) dynamics in the sense that if the numerical scheme behaves well for these three cases, one would expect it to capture, with a comparable accurately, the rich – balanced/unbalanced dispersive/non-dispersive – large scale dynamics of the tropics.

In Table 1, we compare the exact solutions, $U_e = (u_e, v_e, \theta_e)$, as given in (4.8), (4.9), or (4.10), respectively, with their numerical analogues, $U_n = (u_n, v_n, \theta_n)$, computed by the f-wave algorithm using the exact boundary condition in BC#3.

Table 1 L1-norm convergence for the Kelvin , Yanai, and MI = 2 Rossby wave with exact-solution boundary conditions at the zonal walls. CFL = .9 with MC limiter. The relative errors are shown

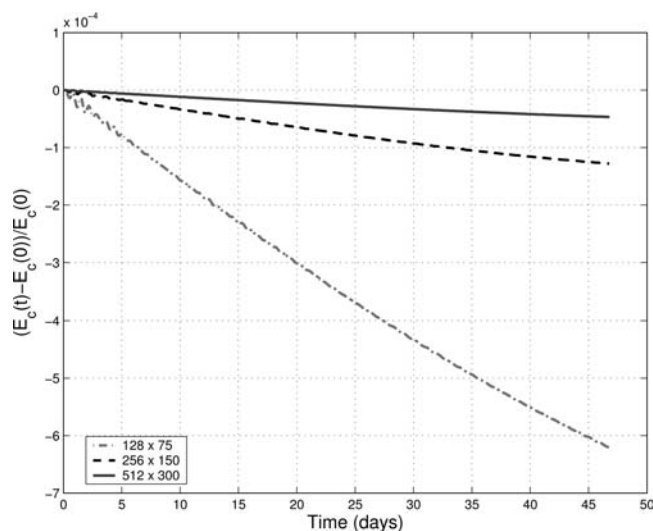| Wave	Integration time	128×75	256×150	512×300
Kelvin (balanced)	2 days	1.0794 E-03	2.6709 E-04	6.6931 E-05
Yanai (unbalanced)	2 days	1.6314 E-03	4.0708 E-04	1.0264 E-04
MI = 2 Rossby (weakly balanced)	47 days	1.6065 E-02	3.9989 E-03	1.0057 E-03

Fig. 1 Relative change of baroclinic energy with time. Computation of MI $= 2$ Rossby wave with the f-wave algorithm. Exact boundary conditions at the zonal walls are used. MC limiter with CFL $= .9$

We report in Table 1 the L1-norm relative errors, $(\int \int |U_n - U_e| dxdy)/(\int \int |U_e| dxdy)$, after an integration time of about two days for the Kelvin and Yanai waves and about 47 days for the MI=2 Rossby wave. Three different grids, 128×75, 256×150, and 512×300 with the CFL number .9 are used. Since these solutions do not develop shocks or discontinuities, the second order accuracy is established with and without (not shown) the MC limiter.

Figure 1 displays the relative change in baroclinic energy for the three runs on the last row of Table 1, for the MI $= 2$ Rossby wave. (The energy plots for the other waves resemble to Fig. 1, therefore there are not shown here). Figure 1, particularly, demonstrates that except for some small numerical dissipation which diminishes with the grid refinement (on the order of at least two), the scheme conserves energy. Before closing this subsection, it is worth mentioning that the discretization errors (not shown) dominate within the interior of the domain at the locations where the wave topological changes are more significant.

4.7 Role of boundary conditions and distance from walls

As noted above the boundary condition BC#3 assumes the knowledge of the solution at the boundaries can be used only for validation purposes. Here, we investigate the effect of practical boundary conditions such as the ones given in BC#1 and BC#2 for the computations of the equatorial waves in a channel. Also we check the sensitivity of the results to the distance between the north and south walls by increasing Y from the more physical value of $Y = 5,000$ km to a more conservative value $Y = 8,000$ km. For brevity we consider only the case of the first symmetric (MI $= 1$) Rossby wave,

$$v(x, y, t) = ye^{-y^2/2} \cos(kx - \omega t)$$
$$q(x, y, t) = \frac{2y^2 - 1}{k - \omega} e^{-y^2/2} \sin(kx - \omega t) \qquad (4.11)$$
$$r(x, y, t) = -\frac{1}{k + \omega} e^{-y^2/2} \sin(kx - \omega t)$$

with ω is the smallest in magnitude root of the dispersion relation

$$\omega^2 - k^2 - \frac{k}{\omega} = 3.$$

Notice that this constitutes an intermediate new test which is harder compared to the Kelvin and Yanai waves because it is less trapped near the equator but perhaps easier than the MI $= 2$ case.

Table 2 Role of boundary conditions and distance from walls for the MI = 1 Rossby wave. L1-norm relative error between exact and computed solution. CFL = .9 with MC limiter are used

Boundary condition	Y (1000 km)	128×75	256×150	512×300
BC#3	5	8.9746 E-03	2.2387 E-03	5.6180 E-04
BC#1	5	1.1349 E-02	7.1270 E-03	8.3801 E-03
BC#2	5	1.3947 E-02	9.2273 E-03	9.7671 E-03
BC#2	8	1.4016E-02	3.4635E-03	8.6216 E-04

In Table 2, we report the L1-norm errors occurred between the exact solution and the numerical solution using the boundary conditions BC#1, BC#2 and BC#3 as well as the results obtained with the boundary conditions BC#2 when the wall distance is increased to $Y = 8000$ km, for the integration time of about 16 days, equivalent to one period. Again the second order convergence is observed with the use of the exact boundary condition BC#3.

However, the rows BC#1 and BC#2 with $Y = 5000$ km in Table 2 demonstrate particularly that the solutions using the non-exact boundary conditions do not converge to the exact equatorial (M = 1) Rossby wave as the error does not decrease with the grid refinement. Nevertheless, the L1-error remains small and as shown on Fig. 2A the tiny errors are confined to a small strip (numerical boundary layer) near the walls. More importantly, as shown on Fig. 2B, the energy remains essentially conserved except for a small transient period where a small deviation from the initial condition due to the use of non-exact boundary conditions occurs. Moreover, the use of a larger wall distance ($Y = 8000$ km) 'circumvents' this boundary condition artifact. In fact, the last row in Table 2 'demonstrates' a second order convergence and the energy plots on Fig. 2D show energy conservation from the beginning. (Except for the expected numerical dissipation, etc. which is nevertheless small and converges to zero with the order two, with the grid refinement.)

The error distribution mesh plot on Fig. 2C shows no numerical boundary layer unlike the panel (a) above it. This clearly demonstrates the role played by the distance from the walls on the approximation of the equatorial waves when using 'artificial' boundary conditions such as in BC#1 and BC#2. Because
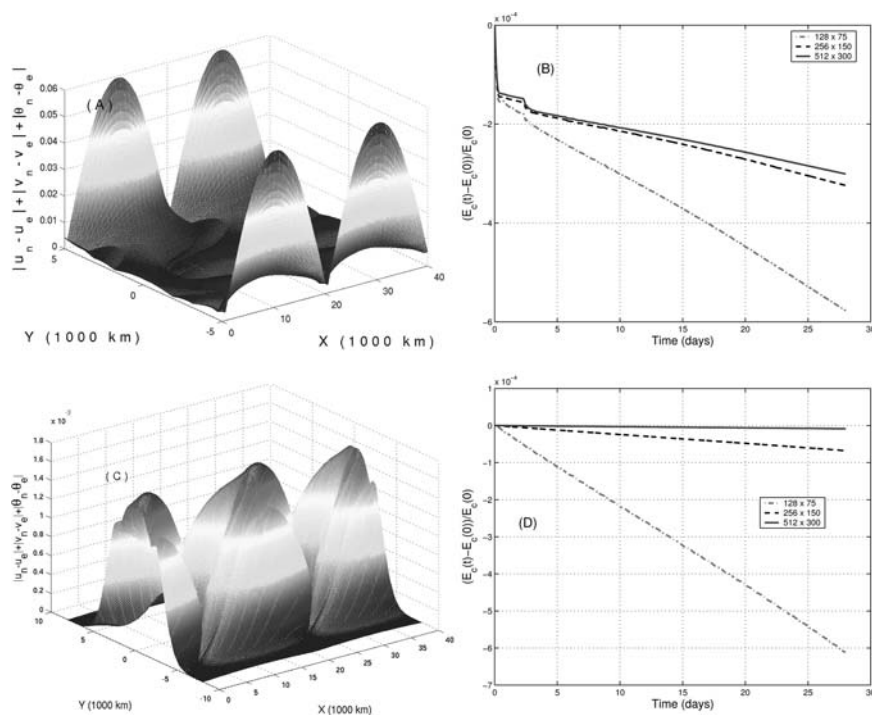

Fig. 2 Role of boundary conditions and distance from walls on the approximation of equatorial waves. Case of MI = 1 Rossby wave with boundary condition BC#2. Error distribution on the finest grid of 512×300: **A** $Y = 5000$ km, **C** $Y = 8000$ km, and energy-time plots with three different grids: **B** $Y = 5000$ km, **D** $Y = 8000$ km

the equatorial waves are trapped at the equator, the further the walls are far from the equator the less the discrepancies between the boundary conditions which are used (e.g., Dirichlet) and the exact solution are important, compared to the second-order error of discretization occurring inside the domain.

5 Non-oscillatory method for barotropic waves

For the barotropic equations in (3.2), we propose to adapt the central scheme introduced and used in [29] by Levy and Tadmor for the 2d incompressible Euler equations. The novelty here is that, unlike the Euler equations, (3.2) supports dispersive (Rossby) waves. As Levy and Tadmor did, we deal directly with the potential vorticity-stream function formulation in (3.3). As noted in [29], the design of the central-incompressible scheme takes a double advantage in the facts that the dynamical equation for the (potential) vorticity can be alternatively written in an advective form as in (3.3) or in the conservative from,

$$\frac{\partial \overline{\xi}}{\partial t} + \frac{\partial}{\partial x}(\overline{u}\overline{\xi}) + \frac{\partial}{\partial y}(\overline{v}\overline{\xi}) = 0, \tag{5.1}$$

thanks to the incompressibility constraint. Recall that while in the discretization of the baroclinic term in Sect. 4, the well balanced scheme is the key to maintaining geostrophic balance, here this problem is solved by going to the vorticity stream-function formulation in (3.4). The conservative form justifies the use of a finite volume method while the advective form guarantees a finite-speed of propagation. The full details of the central-incompressible scheme can be found in [29], we next give a brief summary for the sake of completeness.

5.1 The central incompressible scheme

The two-dimensional central scheme of Nessyahu-Tadmor [29, 33] uses two staggered grids (x_j, y_k) and $(x_{j+1/2}, y_{k+1/2})$ with $x_l = l\Delta x$ and $y_l = l\Delta y$. Given the centered cell averaged values $\xi_{j,k}$ at time t, a finite volume approximation over the control volume $[x_j, x_{j+1}] \times [y_k, y_{k+1}] \times [t, t + \Delta t]$, for a given time step, Δt, permits one to update the staggered cell averages $\xi_{j+1/2,k+1/2}$ at time $t + \Delta t$. The main advantage of the central scheme resides in the fact that the solution is well defined (smooth) at the judiciously chosen cell interfaces (x_j, y), $y_k \leq y \leq y_{k+1}$, and (x, y_k), $x_j \leq x \leq x_{j+1}$, and there is no Riemann problem attached to them, provided Δt is small enough. Therefore the integrals resulting from the finite volume discretization are evaluated by simple quadrature rules. A trapezoidal rule in space (in y for the x-flux and in x for the y-flux) combined with the mid-point formula in time are used. In order to achieve a fully explicit scheme a predictor-corrector strategy using a first order Euler method to estimate the mid-time-step-values is employed. However some special care is taken when reconstructing the staggered cell averages $\xi_{j+1/2,k+1/2}$, at time t, because one has to integrate across the cell interfaces $(x_{j+1/2}, y)$, $y_k \leq y \leq y_{k+1}$, and $(x, y_{k+1/2})$, $x_j \leq x \leq x_{j+1}$, where the cell-average solution (here ξ) is not defined; it has jumps. This is where a non oscillatory 2nd order polynomial interpolation with the MINMOD limiter is used [29].

The central incompressible scheme for the barotropic system in (3.3) is achieved by combining the predictor-corrector central scheme, briefly described above, for the conservation equation of potential vorticity in (5.1) with a solver for the streamfunction Poisson equation with the appropriate differentiation formula which guaranties numerical incompressibility. We use a five-point stencil for the Poisson equation:

$$\frac{\overline{\psi}_{j+1,k} - 2\overline{\psi}_{j,k} + \overline{\psi}_{j-1,k}}{\Delta x^2} + \frac{\overline{\psi}_{j,k+1} - 2\overline{\psi}_{j,k} + \overline{\psi}_{j,k-1}}{\Delta y^2} = \overline{\omega}_{j,k} \equiv (\overline{\xi}_{j,k} - y_k) \tag{5.2}$$

$1 \leq j \leq N, 1 \leq k \leq M$. We solve the difference equation in (5.2) by combining the FFT method for the periodic x-direction and a direct method in y. The details of the semi-direct Poisson solver are skipped since it is quite a standard approach for channel domains. However, it is worth mentioning that in order to close the Poisson equation we use the Neumann boundary condition,

$$\frac{\partial \overline{\psi}}{\partial x}\bigg|_{y=\pm Y} = 0$$

dictated by the no-flow condition in (2.8), which translates immediately to the Fourier modes as a Dirichlet boundary condition except for the mode number one where some special treatment is needed. The Fourier method,

$$\psi_{j,k} = \sum_{l=1}^{N} \hat{\psi}_{l,k} \exp(I(j-1)(l-1)2\pi\Delta x), \quad I^2 = -1$$

applied to the difference equation in (5.2), leads to a tridiagonal system for each Fourier mode with the homogeneous Dirichlet boundary conditions, $\hat{\psi}_{l,0} = \hat{\psi}_{l,M} = 0$, for all the modes, $2 \leq l \leq N$, except for the first mode, $l = 1$, for which the wall constraints on the x-derivative of the streamfunction is trivial. We obtain a boundary condition for the first mode by relying on the conservation of the zonal mean wind at the north-south boundaries. In fact, the zonal averaging of the first momentum equation in (3.3) combined with the no-flow condition in (2.8) leads to

$$\frac{\partial \langle \overline{u} \rangle_x}{\partial t} = 0 \text{ at } y = \pm Y, \tag{5.3}$$

where $\langle f \rangle_x(y,t) = \frac{1}{P} \int_0^P f(x,y,t)dx$ denotes the zonal averaging of the function f. The condition in (5.3) is enforced during the coding of the Poisson solver.

Now, we construct the incompressible flow from the discrete stream-function solution provided by the Poisson solver of (5.2). Simple second order centered finite differences are used.

$$\overline{u}_{j,k} = -\frac{\overline{\psi}_{j,k+1} - \overline{\psi}_{j,k-1}}{2\Delta y}; \quad \overline{v}_{j,k} = \frac{\overline{\psi}_{j+1,k} - \overline{\psi}_{j-1,k}}{2\Delta x}. \tag{5.4}$$

If the second order centered differences are also used to compute the discrete divergence, then we get

$$D_x\overline{u}_{j,k} + D_y\overline{v}_{j,k} \approx \frac{\overline{u}_{j+1,k} - \overline{u}_{j-1,k}}{2\Delta x} + \frac{\overline{v}_{j,k+1} - \overline{v}_{j,k-1}}{2\Delta x}$$

$$= -\frac{\overline{\psi}_{j+1,k+1} - \overline{\psi}_{j+1,k-1} - \overline{\psi}_{j-1,k+1} + \overline{\psi}_{j-1,k-1}}{4\Delta y\Delta x}$$

$$+ \frac{\overline{\psi}_{j+1,k+1} - \overline{\psi}_{j-1,k+1} - \overline{\psi}_{j+1,k-1} + \overline{\psi}_{j-1,k-1}}{4\Delta x\Delta y} \equiv 0,$$

i.e., the discrete flow field, $(\overline{u}_{j,k}, \overline{v}_{j,k})$ obtained in this fashion is incompressible. This is conceptually simpler and computationally cheaper than the centering of the incompressibility at the staggered grid points, $(j + 1/2, k + 1/2)$ employed in [29].

5.2 Boundary conditions for the potential vorticity

One may argue that since the meridional component of the advecting velocity vanishes at the walls the information outside the walls does not propagate into the domain, and therefore any kind of boundary conditions can be used there. However, this turns out to be a mistake. We demonstrate below that the choice of suitable numerical boundary conditions for $\overline{\xi}$ at the walls is crucial. Certain types of boundary conditions such as polynomial extrapolation develop a numerical boundary layer near the walls where unphysical vorticity is generated and amplifies with time. We propose to use instead the fixed Dirichlet boundary conditions for the vorticity,

$$\overline{\omega} \equiv \overline{\xi} - y = 0, \quad y = \pm Y, \tag{5.5}$$

which leads to clean and accurate results. At this points, the reasons for this behavior are not well understood.

Table 3 L1-norm relative error between the exact and the numerical barotropic velocity fields obtained by the incompressible central scheme in a zonal channel using the fixed Dirichlet boundary conditions at the walls. Case of a Rossby wave packet with $k_1 \equiv 1$ and $k_2 \equiv 4$

Grid	5 days	10 days	15 days	20 days
128×75	1.7785 E-01	3.3155 E-01	4.8873 E-01	6.4114 E-01
256×150	9.7375 E-02	1.8130 E-01	2.6999 E-01	3.5633 E-01

5.3 Validation with large scale Rossby wave packets

We consider the Rossby wave packets given by

$$\overline{\psi}(x, y) = \cos(k_1 x - \omega t) \sin(k_2 y) \tag{5.6}$$

with (k_1, k_2) are the zonal and meridional wavenumbers, respectively, and the phase ω is given by the dispersion relation

$$\omega = -\frac{k_1}{k_1^2 + k_2^2}, \tag{5.7}$$

which are exact solutions to the nonlinear barotropic equations in (3.3) (see [20]) with the boundary conditions $\overline{v} = 0$ at the walls if the meridional wavenumber is chosen accordingly as discussed below. The solutions described by (5.6) and (5.7) represent a traveling wave packet which propagates in the zonal direction (parallel to the channel walls) at the speed ω / k_1. We run the barotropic code described above for a fixed period of time T. The (initial) magnitude of the wind is such that

$$\max_{x,y} \sqrt{\overline{u}(x, y, 0)^2 + \overline{v}(x, y, 0)^2} = 5 \text{ m/s}.$$

We fix the meridional wavenumber k_2 so that the associated wavelength matches the width of the channel, given by $2Y = 10,000$ km, thus yielding no-flow across the walls. In the zonal direction, we consider two different wavenumbers: $k_1 = 2\pi/X$ (wavenumber one, sometimes we write $k_1 \equiv 1$) yielding a zonal wavelength equal the total equatorial circumference, $X = 40,000$ km, and $k_1 = 8\pi/X$ ($k_1 \equiv 4$) yielding a zonal wavelength identical to the meridional wavelength fixed by the channel width, thus, resulting in a 'square wave'. Notice that the Rossby wave packet in (5.6) satisfies the Dirichlet boundary condition in (5.5) at grid points lying on the walls but not at the ghost points outside the computational domain. Indeed this type of boundary condition forces the solution to be zero 'at' and beyond the channel walls.

We report in Table 3 the L1-norm relative error, with respect to the velocity field $(\overline{u}, \overline{v})$, between the exact and the numerical solutions computed with two different grids, 128×75 and 256×150, at four consecutive times, 5,10,15, and 20 days, for the case $k_1 = 2\pi/X$ with the fixed Dirichlet boundary conditions in (5.5).

In Fig. 3, we plot a zonal slice of the vorticity at roughly $y = 1600$ km for the exact (solid) and the numerical solutions of Table 3, obtained with the 128×75 (dotted) and 256×150 (dashed) grids. In Fig. 5 we monitor relative change of the associated barotropic kinetic energy in (2.10); the two curves named BC1 on Fig. 5. A comparison of the errors in Table 3 for the two grids suggests that the central incompressible scheme captures the large scale dispersive wave in (5.6) with an overall first order accuracy. Moreover we see from Fig. 3 that the numerical solution over-predicts the phase speed as the dotted and dashed lines in Fig. 3 always show up ahead of the solid line. The y-plots of the L1-norm errors in x-direction for the two grids 128×75 and 256×150 at time $t = 5$ days in Fig. 4 suggest an error accumulation near the channel walls (twice as large as the center) perhaps due to the use of the artificial boundary conditions. The boundary errors then propagate rapidly inside the domain because of the elliptic part of the problem. Nonetheless, the low convergence of the first order, which is probably partly if not simply due to the artificial boundary conditions, as suggested above, is not totally clear at this stage. Further investigation is needed and will be addressed elsewhere. But nevertheless, the energy plots of Fig. 5 demonstrate at least a second order convergence energy-wise (compare the two BC1 curves), where only about 1% of energy is dissipated during the integration period of 20 days, and we believe that is satisfactory in this context given the crudeness of the model.

As noted above, although the meridional flow is assumed to vanish at the walls so that the computational domain does not in principle exchange information with the outside walls, the numerical boundary conditions for the (potential) vorticity can not be arbitrarily chosen and actually constitute a subtle issue. Numerical
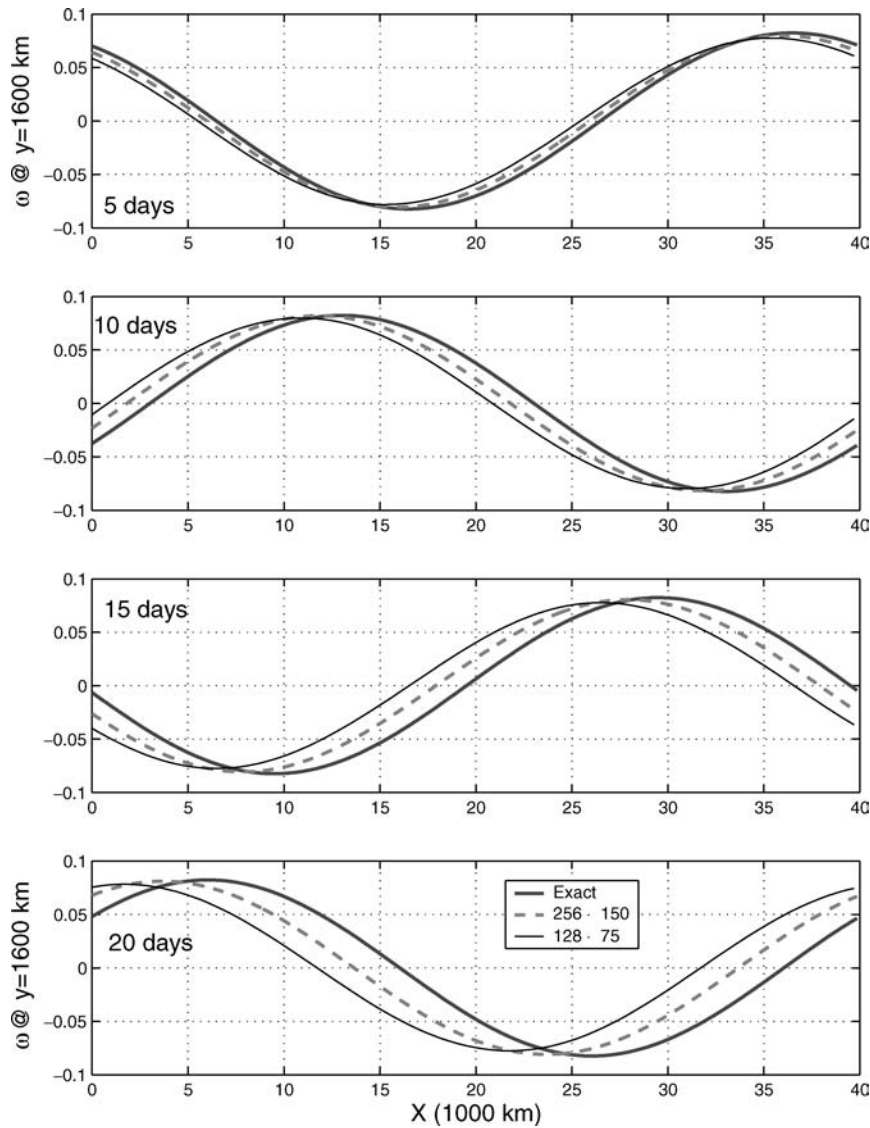
Fig. 3 Zonal slice plots of the vorticity, $\overline{\omega}$, at $y \approx 1600$ km and $t = 5, 10, 15, 20$ days for exact (*thick solid*) and the numerical solutions. Large scale Rossby wave packet with $k_1 \approx 1$, $k_2 \approx 4$. 128×75 (*dotted*) and 256×150 (*thin solid*) grid points

tests revealed that some popular types of boundary conditions such as polynomial extrapolations behave very poorly when compared to the fixed boundary conditions in (5.5). The curves BC2 and BC3 in Fig. 5 represent the energy-time plots obtained for the same large scale Rossby wave when the zero order (constant) and the second order (parabolic) extrapolations to ghost cells (outside the walls) are used, respectively. Compare with the two BC1 curves, which use the Dirichlet boundary condition in (5.5). In Fig. 6 we compare the flow structure of the exact solution (a) and the numerical solutions obtained with the three different boundary conditions listed above for the large scale Rossby wave packet in (5.6) with zonal wavenumber one and meridional wavenumber four at time $t = 20$ days. (The contours are those of the vorticity and the arrows represent the barotropic velocity profiles.) Clearly, overall, the two runs corresponding to the polynomial extrapolation boundary conditions behave very poorly. The vorticity contours of Fig. 6C and D exhibit a numerical boundary layer near the walls and the energy plots in Fig. 5 BC2 and BC3 are less accurate than BC1 in Fig. 6B for the same grid, especially the zero order extrapolation case shows an excessive energy dissipation, almost as bad as the curve obtained by BC1 with the coarse grid of 128×75. Furthermore, while the second order extrapolation seems to be acceptable on the energy side in Fig. 5, the numerical boundary
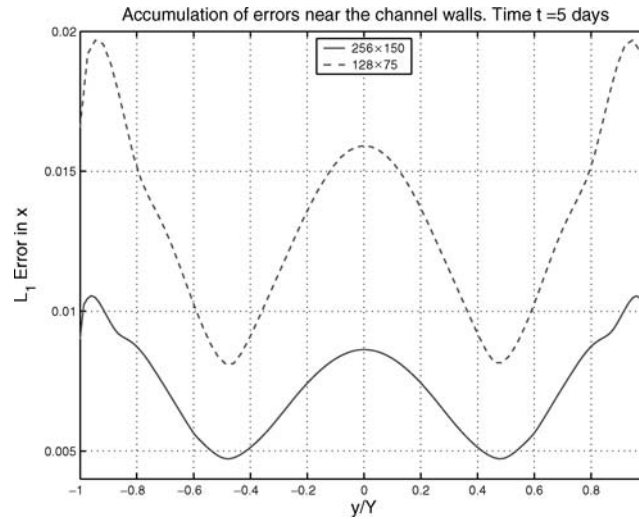
Fig. 4 L1 norm error in x-direction versus y suggesting an accumulation of errors near the channel walls due to the use of artificial boundary conditions
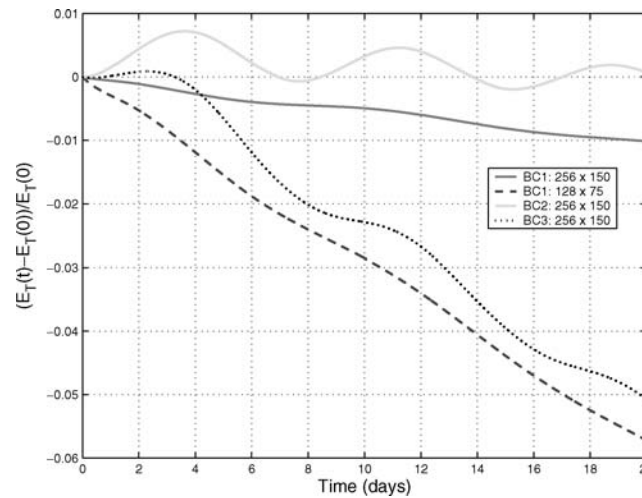

Fig. 5 Barotropic energy-time plots obtained by the incompressible central scheme with the fixed Dirichlet boundary conditions (BC1) using 128×75 and 256×150 grid points and zero order extrapolation (BC2) and second extrapolation (BC3) on a 256×150 grid. Case of a Rossby wave packet with $k_1 \equiv 1$ and $k_2 \equiv 4$

layer seen near the lower wall of Fig. 6D, although narrower than its counterpart in Fig. 5C, displays an enormous unphysical vorticity amplification (roughly by a factor five).

In order to demonstrate that the incompressible central scheme is robust and able to capture dispersive waves with smaller wavelengths, we report in Fig. 7 the results obtained with the higher zonal wavenumber: $k_1 \equiv 4$. Compare the flow structure, at time $t = 20$ days, (contours of the vorticity and velocity arrows) of the exact solution depicted in panel (a) with the numerical solution in panel (b). Notice that the phase shift between the two panels is hardly noticeable, especially for the velocity arrows, as opposed to the larger scale case with $k_1 \equiv 1$ in Fig. 6, so that the dispersion is well captured by the numerical scheme.

6 Concluding discussion

A non-oscillatory geostrophically balanced scheme for a simplified climate model using state of the art numerical methods is proposed. The model is based on a crude vertical resolution reduced to a barotropic and a first baroclinic modes. Nevertheless, such idealized models are widely and successfully used for the studies
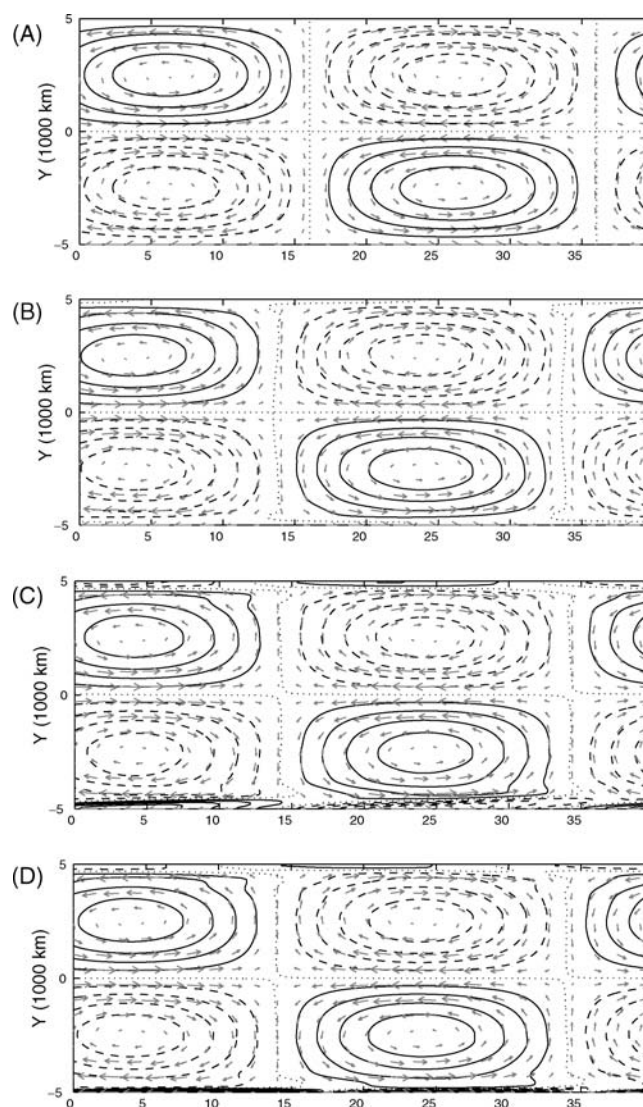
Fig. 6 2d structure of the flow for the Rossby wave packet with $k_1 \equiv 1$ and $k_2 \equiv 4$ at time $t = 20$ days. Contour of the vorticity and velocity profile (arrows). Contour interval 0.02. Solid: positive, Dash: negative, Dots: zero. Exact solution **A** and central incompressible scheme with fixed Dirichlet **B**, zero order extrapolation **C**, and second order extrapolation **D** boundary conditions at the walls. Max (Min) of vorticity on lower boundary of lower panel is .32 $(-.32)$

of the interactions between midlatitude and equatorial Rossby waves as well, since they form an useful tool for the validation and the assessment of convective parametrizations. The non-oscillatory balanced numerical model is suggested as a complementary alternative to the existing balanced asymptotic models such as the WTG and the multiscale models. The barotropic/baroclinic model consists of a highly nonlinear interacting system which conserves total energy in the absence of convective heating and frictional forcing and when suitable boundary conditions are used. We consider a zonally periodic channel centered at the equator with no-flow boundary conditions at the longitudinal walls. We adapt a basic discretization strategy consisting of fractional stepping–operator splitting of the interacting system into three different subsystems which independently conserve energy: A shallow water system for the advected-baroclinic waves, an incompressible barotropic system, and a third system gathering the nonlinear interaction terms.

The advection is present in both the baroclinic and the barotropic subsystems but, however, as a consequence of the Galerkin projecting, it is restricted to the advection by the incompressible barotropic flow, therefore, yielding a (linear) baroclinic subsystem which is written as a system of conservation laws with source terms; the Coriolis forces. We use the f-wave algorithm, proposed by Bale et al. [25] for conservation
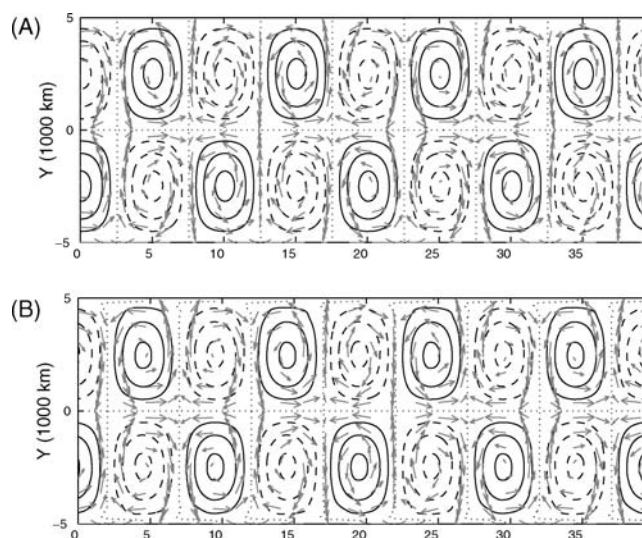
Fig. 7 Same as in Fig. 6 but with a zonal wavenumber $k_1 \equiv 4$. Contour interval 0.04. Exact solution **A** and numerical solution with Dirichlet boundary conditions **B**

laws with varying flux functions and source terms, to discretize the advected baroclinic waves system. The validation tests, in Sect. 4, using known exact solutions among the large scale equatorial waves, such as the Kelvin, the Yanai, and the Rossby waves of index one and two, have confirmed the second order accuracy of the balanced scheme, as demonstrated by the L1-norm errors in Table 1 and the energy plots in Fig. 1. The judiciously chosen validation tests among which we have non-dispersive (Kelvin) and dispersive (Yanai and Rossby) as well as geostrophically balanced (Kelvin), weakly balanced (Rossby), and unbalanced (Yanai) waves, form a representative set of the complex tropical wave dynamics.

We also looked at the effect of the boundary conditions for a flow confined into a channel, such as the non-reflecting and the homogeneous Dirichlet boundary conditions at the channel walls, on these natural exact solutions of the equatorial beta-plane shallow water equations. It turns out that with the physical equator-wall distance of $Y = 5000$ km, for the range of grid mesh sizes varying from about 300 down to 70 km in x and from about 130 down to 30 km in y, the L1-norm between the exact solution and the numerical solution for the large scale $MI = 1$ Rossby wave with the artificial boundary conditions listed above, although it remains very small (less than 1%); it does not decrease significantly with grid refinement, as shown in Table 2. Nevertheless, as demonstrated in Fig. 2A, these small errors are confined near the channel walls where the artificial boundary conditions were imposed. More importantly, as shown in Fig. 2B, the energy is essentially conserved as the numerical dissipation is negligibly small and seem to be controlled (behave well) under grid refinement. A more conservative wall distance of $Y = 8000$ km permits one to recover the second order accuracy in both the L1-norm errors in Table 2 and the energy plots in Fig. 2D. The error distribution plot, for this case with $Y = 8000$, showing an overall error, with the finest grid, concentrated away from the walls as a result of the trapping effect, provides an explanation to why the second order accuracy is recovered and suggests that the channel geometry with a sufficiently large wall distance with either the non-reflecting or the Dirichlet boundary conditions yields an accurate numerical model for the interactions of the equatorially trapped waves of all nature.

It is demonstrated here that the non-oscillatory central scheme, introduced by Levy and Tadmor for the incompressible Euler equations, constitutes an accurate computational tool for the dispersive-barotropic Rossby waves in a channel. The validation tests of Sect. 5, using Rossby wave packets as exact solutions have confirmed this. Due to the use of artificial boundary conditions, the L1-norm errors displayed in Table 3 demonstrates that we have roughly a first order convergence with grid refinement but, nevertheless, the solid and dashed curves among the energy plots in Fig. 5 show that we have at least a second order convergence energy-wise. The first order convergence, is well reflected from the vorticity slices shown in Fig. 3, which demonstrates clearly that the numerical scheme over-predicts the phase speed of the wave packet as we see the dashed and dotted lines always show up at the front and Fig. 4 provides enough evidence to believe that this low convergence behavior is due to the use of artificial boundary conditions at the walls. It is also demonstrated that the naive use of polynomial extrapolation leads to catastrophic generation and amplification of

vorticity within a numerical boundary layer near the channel walls as well as an excessive dissipation of energy, at least for the case with zero order extrapolation.

The overall algorithm developed here is applied in the companion part II of this paper in two different situations. The first example concerns highly non-linear dynamics of interacting baroclinic-barotropic solitary wave solutions to the dry system, as recently discovered by Biello and Majda [34]. The second application looks at the moisture effects through the interactions of the precipitation fronts of Frierson et al. [24] with a barotropic trade wind and the equatorial Coriolis force (beta effect).

Appendix: Wave propagation algorithm for conservation laws

The wave-propagation algorithm for a conservation law,

$$U_t + F(U) = 0,$$

consists on rewriting the left and right fluxes, $F(U^*_{i\pm1/2})$, of the associated finite-volume discretization,

$$U_i^{n+1} = U_i^n - \frac{\Delta t}{\Delta x}[F(U^*_{i+1/2}) - F(U^*_{i-1/2})], \tag{A1}$$

with $U^*_{i-1/2}$ is the solution to the Riemann problem at the interface $i - 1/2$ with the left and right states U_{i-1} and U_i, respectively, as a linear combinations of right- and left-going simple waves. The resulting algorithm is summarized below through the following abstract formulation:

$$U_i^{n+1} = U_i^n - \frac{\Delta t}{\Delta x}[\mathcal{A}^+(\Delta U_{i-1/2}) + \mathcal{A}^-(\Delta U_{i+1/2})] \tag{A2}$$

where $\mathcal{A}^{\pm}(\Delta U_{i-1/2})$ represent respectively the left $(-)$ and right $(+)$ going fluxes across the edge $i-1/2$ with the flux increment

$$F(U_i) - F(U_{i-1}) = \mathcal{A}^+(\Delta U_{i-1/2}) + \mathcal{A}^-(\Delta U_{i-1/2})$$

and

$$\Delta U_{i-1/2} = U_i - U_{i-1}$$

is the wave increment or the jump across $i - 1/2$. Notice that $\mathcal{A}^+(\Delta U_{i-1/2})$ changes the values of the vector U_i while $\mathcal{A}^-(\Delta U_{i-1/2})$ changes the values of U_{i-1}. For a hyperbolic system the jump $U_i - U_{i-1}$ is decomposed onto M waves (typically $M = n$, the dimension of the system), $\mathcal{W}^p_{i-1/2}$, $p = 1, 2, \ldots M$ propagating with the speeds $\lambda^p_{i-1/2}$, $p = 1, 2, \ldots, M$:

$$U_i - U_{i-1} = \sum_{p=1}^{M} \mathcal{W}^p_{i-1/2},$$

which yields

$$F(U_i) - F(U_{i-1}) = \sum_{p=1}^{M} \lambda^p_{i-1/2} \mathcal{W}^p_{i-1/2}.$$

Here $\lambda^p_{i-1/2}$ are the eigenvalues of (some approximation of) the Jacobian matrix $\partial F(U)/\partial U$ (Roe Matrix) and the waves $\mathcal{W}^p_{i-1/2}$ are the projection onto the associated eigenvectors. The flux-difference scheme in (A2) is then closed by setting

$$\mathcal{A}^-(\Delta U_{i-1/2}) \equiv \sum_{p=1}^{M} \left(\lambda^p_{i-1/2}\right)^- \mathcal{W}^p_{i-1/2}$$

$$\mathcal{A}^+(\Delta U_{i-1/2}) \equiv \sum_{p=1}^{M} \left(\lambda^p_{i-1/2}\right)^+ \mathcal{W}^p_{i-1/2} \tag{A3}$$

where $\lambda^+ = \max(\lambda, 0)$ and $\lambda^- = \min(\lambda, 0)$.

The second orderr extension in the context of the wave algorithm is obtained by adding on the right hand side of the updating formula in (A2) the appropriate wave correction terms, yielding [26]

$$U_i^{n+1} = U_i^n - \frac{\Delta t}{\Delta x}[\mathcal{A}^+(\Delta U_{i-1/2}) + \mathcal{A}^-(\Delta U_{i+1/2})] - \frac{\Delta t}{\Delta x}(\tilde{F}_{i+1/2} - \tilde{F}_{i-1/2}), \tag{A4}$$

where the second order correction $\tilde{F}_{i-1/2}$ is given by

$$\tilde{F}_{i-1/2} = \frac{1}{2} \sum_{p=1}^{M} |\lambda_{i-1/2}^{p}| \left(1 - \frac{\Delta t}{\Delta x} |\lambda_{i-1/2}^{p}|\right) \tilde{\mathcal{W}}_{i-1/2}^{p}$$

with

$$\tilde{\mathcal{W}}_{i-1/2}^{p} = limiter\left(\mathcal{W}_{i-1/2}^{p}, \mathcal{W}_{I-1/2}^{p}\right), \quad I = \begin{cases} i-1 & \text{if } \lambda_{i-1/2}^{p} > 0 \\ i+1 & \text{if } \lambda_{i-1/2}^{p} < 0. \end{cases}$$

Here *limiter* is the flux limiting function leading to a non-oscillatory scheme, which is specified in the code. We actually use the monotonized central (MC) limiter (see for e.g., [35]).

References

1. Majda, A., Biello, J.: The nonlinear interaction of barotropic and equatorial baroclinic Rossby waves. J. Atmos. Sci. **60**, 1809–1821 (2003)
2. Biello, J., Majda, A.: Boundary layer dissipation and the nonlinear interaction of equatorial baroclinic barotropic Rossby waves. Geophysical and Astrophysical Fluid Dynamics **98**, 85–127 (2004)
3. Webster, P.: Response of the tropical atmosphere to local steady forcing. Mon. Wea. Rev. **100**, 518–541 (1972)
4. Webster, P.: Mechanisms determining the atmospheric response to sea surface temperature anomalies. J. Atmos. Sci. **38**, 554–571 (1981)
5. Webster, P.: Seasonality in the local and remote atmospheric response to sea surface temperature anomalies. J. Atmos. Sci. **39**, 41–52 (1982)
6. Kasahara, A., Silva Dias, P.: Response of planetary waves to stationary tropical heating in a global atmosphere with meridional and vertical shear. J. Atmos. Sci. **43**, 1893–1911 (1986)
7. Hoskins, B., Jin, F.-F.: The initial value problem for tropical perturbations to a baroclinic atmosphere. Quart. J. Roy. Meteor. Soc. **117**, 299–317 (1991)
8. Wang, B., Xie, X.: Low-frequency equatorial waves in vertically sheared zonal flow. Part I: Stable waves. J. Atmos. Sci. **53**, 449–467 (1996)
9. Chiang, J., Sobel, A.: Tropical tropospheric temperature variations caused by enso and their influence on the remote tropical climate. J. Atmos. Sci. **15**, 2616–2631 (2002)
10. Emanuel, K.: An air-sea interaction model of intraseasonal oscillations in the tropics. J. Atmos. Sci. **44**, 2324–2340 (1987)
11. Neelin, D., Held, I., Cook, K.: Evaporation-wind feedback and low frequency variability in the tropical atmosphere. J. Atmos. Sci. **44**, 2341–2348 (1987)
12. Goswami, P., Goswami, B.: Modification of $n = 0$ equatorial waves due to interaction between convection and dynamics. J. Atmos. Sci. **48**, 2231–2244 (1991)
13. Yano, J.-I., Emanuel, K.: An improved model of the equatorial troposphere and its coupling to the stratosphere. J. Atmos. Sci. 377–389 (1991)
14. Neelin, D., Yu, J.: Modes of tropical variability under convective adjustment and the Madden-Julian Oscillation. Part I: Analytical theory. J. Atmos. Sci. **51**, 1876–1894 (1994)
15. Majda, A., Shefter, M.: Waves and instabilities for model tropical convective parametrizations. J. Atmos. Sci. **58**, 896–914 (2001)
16. Lin, W.-B., Neelin, D., Zeng, N.: Maintenance of tropical intraseasonal variability: Impact of evaporation-wind feedback and midlatitude storms. J. Atmos. Sci. **57**, 2793–2823 (2000)
17. Neelin, D., Zeng, N.: A quasi-equilibrium tropical circulation model–formulation. J. Atmos. Sci. **57**, 1741–1766 (2000)
18. Yano, J.-I., Moncrieff, M., McWilliams, J.: Linear stability and single-column analyses of several cumulus parametrization categories in a shallow-water model. Quart. J. Roy. Meteor. Soc. **124**, 983–1005 (1998)
19. Gill, A.: Atmosphere-Ocean Dynamics. International Geophysics Series, Vol. 30. Academic Press (1982)
20. Majda, A.: Introduction to PDEs and Waves for the Atmosphere and Ocean. Courant Lecture Notes, Vol. 9. Amer. Mat. Soc. (2003)
21. Wheeler, M., Kiladis, G.: Convectively coupled equatorial waves: Analysis of clouds and temperature in the wavenumber-frequency domain. J. Atmos. Sci. **56**, 374–399 (1999)
22. Sobel, A., Nilsson, J., Polvani, M.: The weak temperature gradient approximation and balanced tropical moisture waves. J. Atmos. Sci. **58**, 3650–3665 (2001)
23. Majda, A., Klein, R.: Systematic multiscale models for the tropics. J. Atmos. Sci. **60**, 393–408 (2003)
24. Frierson, D., Majda, A., Pauluis, O.: Dynamics of precipitation fronts in the tropical atmosphere. Comm. Math. Sciences, 2, No.4 (2004)
25. Bale, D., LeVeque, R., Mitran, S., Rossmanith, J.: A wave propagation method for conservation laws and balance laws with spatially varying flux functions. SIAM Jour. Sci. Comput. **24**, 955–978 (2002)
26. LeVeque, R.: Balancing source terms and flux gradients in high-order Godunov methods: The quasi-steady wave-propagation algorithm. J. Comput. Phys. **146**, 346–365 (1998)
27. Audusse, E., Bouchut, F., Bristeau, M.-O., Klein, R., Perthame, B.: A fast and stable well-balanced scheme with hydrostatic reconstruction for shallow water flows. SIAM Jour. Sci. Comput. **25**, 2050–2065 (2004)
28. Bouchut, F., Le Sommer, J., Zeitlin, V.: Frontal geostrophic adjustment and nonlinear wave phenomena in one dim rotating shallow water: part 2: high resolution numerical simulations. J. Fluid Mech. in press (2004)
29. Levy, D., Tadmor, E.: Non-oscillatory central schemes for the incompressible 2-D Euler equations. Mathematical Research Letters **4**, 1–20 (1997)

30. Kupferman, R., Tadmor, E.: A fast, high resolution, second-order central scheme for incompressible flows. Proc. Nat. Acad. Sci. **94**, 4848–4852 (1997)
31. Durran, D.: Numerical Methods for Wave Equations in Geophesical Fluid Dynamics. Springer-Verlag, NY (1999)
32. Evans, L.: Partial differential equations, Graduate Studies in Mathematics, Vol. 19, Amer. Math. Soc. (1998)
33. Zhang, Z.-C., John Yu, S.: A non oscillatory central scheme for conservation laws. In: AIAA Fluid Dynamics Conference, 30th, June 28–July 1, AIAA-1999-3576 Norfolk, VA (1999)
34. Biello, J., Majda, A.: The effect of meridional and vertical shear on the interaction of equatorial baroclinic and barotropic Rossby waves. Studies in App. Math. **112**, 341–390 (2003)
35. LeVeque, R.: Numerical Methods for Conservation Laws. Birkhäuser, Basel (1990)